

# Magnetic excitations and anomalous spin wave broadening in multiferroic $\text{FeV}_2\text{O}_4$

Qiang Zhang,<sup>1,2</sup> Mehmet Ramazanoglu,<sup>1,2</sup> Songxue Chi,<sup>3</sup> Yong Liu,<sup>1</sup> Thomas. A. Lograsso,<sup>1,4</sup> and David Vaknin<sup>1,2</sup>

<sup>1</sup>Ames Laboratory, Ames, IA, 50011, USA

<sup>2</sup>Department of Physics and Astronomy, Iowa State University, Ames, IA, 50011, USA

<sup>3</sup>Oak Ridge National Laboratory, Oak Ridge, Tennessee 37831, USA

<sup>4</sup>Division of Materials Sciences and Engineering, Iowa State University, Ames, Iowa 50011, USA

(Dated: July 10, 2021)

We report on the different roles of two orbital-active  $\text{Fe}^{2+}$  at the A site and  $\text{V}^{3+}$  at the B site in the magnetic excitations and on the anomalous spin wave broadening in  $\text{FeV}_2\text{O}_4$ .  $\text{FeV}_2\text{O}_4$  exhibits three structural transitions and successive paramagnetic (PM)-collinear ferrimagnetic (CFI)-noncollinear ferrimagnetic (NCFI) transitions. The high-temperature tetragonal/PM -orthorhombic/CFI transition is accompanied by the appearance of an energy gap with a high magnitude in the magnetic excitations due to strong spin-orbit coupling induced anisotropy at the  $\text{Fe}^{2+}$  site. While there is no measurable increase in the energy gap from the orbital ordering of  $\text{V}^{3+}$  at the orthorhombic/CFI-tetragonal/NCFI transition, anomalous spin wave broadening is observed in the orthorhombic/CFI state due to  $\text{V}^{3+}$  spin fluctuations at the B site. The spin wave broadening is also observed at the zone boundary without softening, which is discussed in terms of magnon-phonon coupling.

Understanding the orbital degrees of freedom and their coupling with spin and lattice degrees of freedom has emerged as a forefront topic in modern condensed-matter physics as these coupled degrees of freedom play a central role in inducing novel phenomena[1]. Vanadium spinel oxides with formula  $\text{AV}_2\text{O}_4$  are ideal systems to study the orbital ordering (OO) by virtue of the fact that the  $3d^2$  high-spin configuration of  $\text{V}^{3+}$  is accommodated in the triply degenerate  $t_{2g}$  states rendering it with orbital degrees of freedom. For a non-magnetic occupancy of the A site by a divalent ion such as Zn, Mg and Cd [2], there is usually a structural transition from cubic to tetragonal, followed by a magnetic ordering at a lower temperature. Replacing A by a magnetic ion  $\text{Mn}^{2+}$  in a  $3d^5$  high spin configuration without orbital degrees of freedom leads to different magnetic transitions although there exists a similar structural transition: a paramagnetic (PM)-collinear ferrimagnetic (CFI) in the same cubic symmetry at  $T_{N1} \approx 56$  K, followed by a CFI-noncollinear ferrimagnetic (NCFI) transition accompanied by the cubic-tetragonal structural transition at  $T_{N2} \approx 53$  K. In  $\text{FeV}_2\text{O}_4$ , the A-site  $\text{Fe}^{2+}$  with a high-spin  $3d^6$  configuration and three electrons in the doubly degenerate  $e$  states gives rise to orbital degrees of freedom of  $\text{Fe}^{2+}$ [1, 4].  $\text{FeV}_2\text{O}_4$  exhibits similar PM-CFI-NCFI transitions as in  $\text{MnV}_2\text{O}_4$ , but the competition or cooperation between two orbital-active  $\text{Fe}^{2+}$  and  $\text{V}^{3+}$  leads to controversial three[2, 3] or four structural transitions[1]. Previous investigations have focused on the orbital ordering of  $\text{V}^{3+}$  at the B site and its effect on the cubic-tetragonal transition and the magnetic excitations in  $\text{AV}_2\text{O}_4$  ( $A = \text{Zn, Mg, Cd and Mn}$ ).[7–11]  $\text{FeV}_2\text{O}_4$  provides a good candidate to investigate the roles of orbital orderings on both sites. Recent discovery of multiferroicity in  $\text{FeV}_2\text{O}_4$  [2, 5], in coexistence of ferroelectricity and noncollinear ferrimagnetism in contrast to the antiferromagnetism in most of the multiferroics, further

motivates us to focus on this system. The ferroelectricity is not found in the collinear ferrimagnetic phase and only emerges in the noncollinear ferrimagnetic phase. It is of interest to compare the spin dynamics [13] in these two distinct magnetic phases, and also to figure out the source of the spin frustration in  $\text{FeV}_2\text{O}_4$  since spin frustration is usually related to the appearance of the ferroelectricity in various noncollinear magnetic phases [14, 15]. Here, we report elastic and inelastic neutron scattering results on high-quality  $\text{FeV}_2\text{O}_4$  single crystal.

The experimental details and the schematic evolution of the structure based on the splittings of the (400) Bragg peak in the cubic setting are provided in the “Supplemental Material”. The obtained lattice constants as a function of temperature shown in Fig. 1 (a) indicate that there are three structural transitions: cubic-high-temperature (HT) tetragonal ( $c < a$ ) at  $T_S = 140$  K, HT tetragonal-orthorhombic at  $T_{N1} = 110$  K, orthorhombic-low-temperature (LT) tetragonal at  $T_{N2} = 70$  K and no other tetragonal-orthorhombic structural transition at  $\approx 35$  K as reported by Katsufuji *et al.* [1] but not by others[3, 4]. Figure 1(b) shows the temperature dependence of the DC susceptibility after zero-field-cooling and field-cooling (FC) in magnetic field of 1000 Oe parallel to the [111]. Below  $T_{N1}$ , a rapid increase in the susceptibility is ascribed to the PM to CFI ordering where the  $\text{Fe}^{2+}$  moments are parallel to [001] and the  $\text{V}^{3+}$  moments are antiparallel to  $\text{Fe}^{2+}$  moments via antiferromagnetic coupling  $J_{\text{Fe-V}}$  [2, 3]. Another jump in the FC susceptibility below  $T_{N2}$  results from CFI to NCFI transition due to the  $\text{V}^{3+}$  canting [2, 3] along any of  $\langle 111 \rangle$  directions.[3]. The schematic CFI and NCFI magnetic structures projected on the  $ac$  plane with the main magnetic interactions[2, 3] are shown in Fig. 1(d). The inverse susceptibility shows a deviation below  $T_S$ , indicating a magnetoelastic coupling [1] at  $T_S$ . We note that  $\text{FeCr}_2\text{O}_4$  with only orbital-active  $\text{Fe}^{2+}$  exhibits sim-

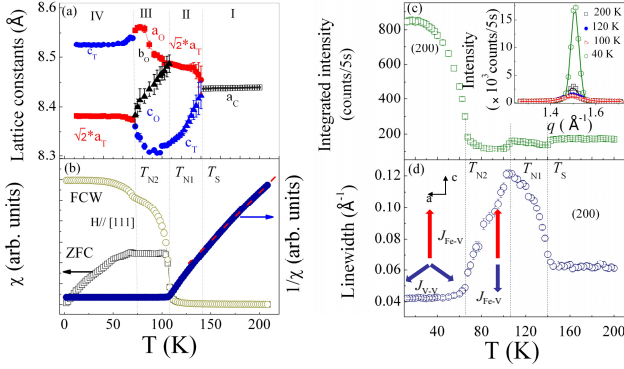


Figure 1: (color online) (a) Temperature dependence of the lattice parameters in  $\text{FeV}_2\text{O}_4$ . (b) Temperature dependence of the DC susceptibility (squares) after zero-field-cooled and field-cooled with  $H//[111]$  axis in  $\text{FeV}_2\text{O}_4$ . The solid circles show the inverse susceptibility. Temperature dependence of (c) the integrated intensity and (d) linewidth of (200) peak. The inset of (c) shows representative  $q$  scans of the (200) peak. The solid lines are fits to a Gaussian function. The schematic magnetic structures projected on the  $ac$  plane with the main magnetic interactions below/above  $T_{N2}$  are also shown in (d). The long arrows and short arrows represent  $\text{Fe}^{2+}$  and  $\text{V}^{3+}$  spins, respectively. Three dashed lines mark the three transitions.

ilar PM cubic-PM tetragonal ( $c < a$ )-CFI orthorhombic transitions [17] without the lowest one at  $T_{N2}$ . Thus, the two transitions at  $T_S$  and  $T_{N1}$  in  $\text{FeV}_2\text{O}_4$  are mainly ascribed to the involvement of orbital-active  $\text{Fe}^{2+}$ . [4] The LT tetragonal phase with  $c > a$  in  $\text{FeV}_2\text{O}_4$  is unique in all the vanadium spinel oxides, suggesting both orbital-active  $\text{Fe}^{2+}$  and  $\text{V}^{3+}$  are necessary [1] to induce the third structural transition at  $T_{N2}$ .

Figure 1 (c) and (d) show the temperature dependence of integrated intensity and peak line-width of the high-symmetry-cubic-forbidden (200) reflection in  $\text{FeV}_2\text{O}_4$ . The peak is present at all measured temperatures and exhibits anomalies at the three transitions. We note that the observed (200) is not due to  $\lambda/2$  leakage as the PG filters remove this higher order wavelength to better than one part in  $3 \times 10^6$  as measured on the nuclear (220) Bragg peak and the forbidden (110) at 200 K. The observed (200) peak above  $T_S$  at 200 K has a pure structural origin due to anisotropy of the local environment around the transition-metal atoms with no contribution from charge-ordering (CO) or OO, as discussed in other spinels, such as  $A\text{Fe}_2\text{O}_4$  ( $A = \text{Mn}, \text{Co}$  and  $\text{Fe}$ ) [18]. Whereas weak anomalies at  $T_S$  and  $T_{N1}$  in the intensities and linewidths are present, the (200) reflection with higher intensity and sharper peak below  $T_{N2}$  is mainly magnetic in origin, which confirms the occurrence of  $\text{V}^{3+}$  spin canting as depicted in Fig. 1 (d).

Constant- $\mathbf{Q}$  energy scans were measured at the zone center (220) at various temperatures and at various  $\mathbf{Q}$ 's

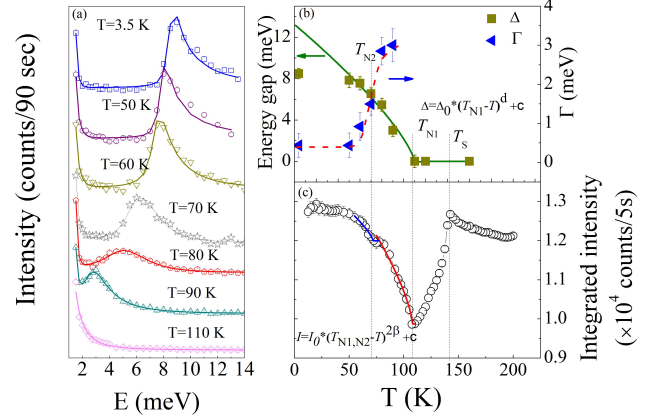


Figure 2: (color online) (a) Constant- $\mathbf{Q}$  energy scans measured at the zone center (220) at various temperatures. The solid lines are fits using the model described in the text. (b) Temperature dependence of (b) the energy gap, damping factor  $\Gamma$ , and (c) the integrated intensity of (220) Bragg peak. The solid lines are fits to the data (see text for more details).

along  $[H H 0]$  at CFI (90K) and NCFI (3.5 K) phases. As shown in Fig. 2 (a), a clear energy gap  $\approx 8$  meV at (220) in low- $E$  region is observed at 3.5 K and the gap drops smoothly with increasing temperature. In the damped simple harmonic oscillator approximation [19–21], the neutron scattering cross-section is given by :

$$\frac{d^2\sigma}{d\Omega dE}(\mathbf{q}, E) \propto \frac{A_q \Gamma E}{[E^2 - (\hbar\omega(\mathbf{q}))^2]^2 + \Gamma^2 E^2} (1 - e^{-E/kT})^{-1} \quad (1)$$

where  $A_q$  is  $q$ -dependent intensity,  $\Gamma$  is spin wave damping factor and can also characterize the intrinsic magnon width,  $(1 - e^{-E/kT})^{-1}$  is the Bose factor. In the small- $\mathbf{q}$  limit, the spin waves around (220) zone center can be approximately described by an anisotropic linear dispersion relation [10, 19]:

$$\hbar\omega(\mathbf{q}) = \sqrt{\Delta^2 + \nu_{ab}^2(q_x^2 + q_y^2)} \quad (2)$$

where  $\nu$  is the spin-wave velocity and  $\Delta$  is the energy gap. The constant- $\mathbf{Q}$  energy scans have been fitted using Eqs. (1) and (2) after convolution with the instrumental resolution using the RESLIB program [22].

The temperature dependence of the energy gap at (220) zone center is shown in Fig. 2 (b). Compared with the behavior of the energy gap in  $\text{MnV}_2\text{O}_4$  [10] where only V has orbital degrees of freedom,  $\text{FeV}_2\text{O}_4$  shows three main differences: 1). In  $\text{FeV}_2\text{O}_4$  the gap emerges below  $T_{N1}$  whereas for  $\text{MnV}_2\text{O}_4$  it only emerges below  $T_{N2}$  ( $= 53$  K); 2). The gap in  $\text{FeV}_2\text{O}_4$  is much higher; 3). No obvious increase in the energy gap ( $\approx 1.5$  meV) as observed in  $\text{MnV}_2\text{O}_4$  is found in  $\text{FeV}_2\text{O}_4$  below  $T_{N2}$ .

In the temperature range  $T_{N2} < T < T_{N1}$  for both  $\text{MnV}_2\text{O}_4$  and  $\text{FeV}_2\text{O}_4$ , the magnetic structures are sim-

ilar without OO of  $V^{3+}$ . [4] The main difference in this temperature region between these two systems is that  $Fe^{2+}$  is orbital-ordered whereas  $Mn^{2+}$  is not. Thus, the appearance of an energy gap below  $T_{N1}$  in  $FeV_2O_4$  is due to the involvement of  $Fe^{2+}$  OO and not related to  $V^{3+}$  ions. It has been shown that the sole PM-CFI magnetic transition without any OO cannot induce an energy gap in  $MnV_2O_4$  [10]. Furthermore, the sole ferroic  $Fe^{2+}$   $3z^2-r^2$  OO [4] does not induce the energy gap below  $T_{N1}$  since the OO is formed at a higher temperature  $T_S$ . Therefore, the spin-orbit coupling induced anisotropy at the A-site  $Fe^{2+}$  is responsible for the appearance of the gap. High-resolution synchrotron x-ray measurements on  $FeV_2O_4$  [4] have shown that there is a strong spin-orbit coupling at the A-site  $Fe^{2+}$  and the CFI ordering below  $T_{N1}$  triggers the structural transition to orthorhombic with a lower symmetry via it, similar to  $ACr_2O_4$  ( $A = Fe, Cu$ ) with only orbital-active ion at the A site [17]. Compared with  $MnV_2O_4$ , the much higher energy gap in  $FeV_2O_4$  results from stronger spin-orbit coupling at  $Fe^{2+}$  A site than that of the  $V^{3+}$  B site in  $MnV_2O_4$ . The larger ordered moment of  $4.0 \mu_B$  [3] of  $Fe^{2+}$  below  $T_{N1}$  than that of the V ion ( $1.3 \mu_B$ ) in  $MnV_2O_4$  [10] also contributes to the higher gap. Below  $T_{N2}$ , although spin ordering of  $V^{3+}$  are similar and  $V^{3+}$  becomes orbital-ordered in both  $MnV_2O_4$  and  $FeV_2O_4$ , the absence of measurable increase in energy gap below  $T_{N2}$  in  $FeV_2O_4$  implies nearly quenched orbital moments or a very weak SO coupling for the  $V^{3+}$ , consistent with soft x-ray magnetic circular dichroism experiments [23] and theoretical calculations [4].

To further get insight into the temperature evolution of the energy gap, we performed a least-square fit using power law  $\Delta(T) \propto (T_{N1} - T)^d$  and obtained an exponent  $d \approx 0.75$  below  $T_{N1}$ , similar to the value of  $\approx 0.73$  in  $MnV_2O_4$  below  $T_{N2}$ . [10] This indicates the the energy gap induced by the anisotropy at  $Fe^{2+}$  site in  $FeV_2O_4$  has similar temperature evolution and critical behavior as the energy gap due to the anisotropy at  $V^{3+}$  B site in  $MnV_2O_4$ . We also modeled the temperature dependence of the integrated intensity of Bragg peak (220) around  $T_{N1}$  and  $T_{N2}$  using  $I(T) \propto (T_{N1,N2} - T)^{2\beta}$ , yielding critical exponents  $\beta_1 \approx 0.353$  at  $T_{N1}$  and  $\beta_2 \approx 0.381$  at  $T_{N2}$ . This indicates that  $FeV_2O_4$  is close to the 3D Heisenberg ( $\beta = 0.36$ ) or 3D Ising ( $\beta = 0.33$ ) models. These two critical exponents are similar to the values near  $T_{N1}$  and  $T_{N2}$  reported in  $MnV_2O_4$  [10]. The comparison of  $\beta_1$  with  $d$  values below  $T_{N1}$  in  $FeV_2O_4$  indicates that the temperature dependence of the energy gap varies like the square of the staggered magnetization [10] once the CFI ordering sets in.

We emphasize that the spin wave damping factor  $\Gamma$  (see Fig. 2 (b)) increases rapidly at  $T_{N2}$ . We also used the Lorentz function convoluted with spectrometer resolution function to model constant- $\mathbf{Q}$  energy scans yielding FWHM values very close to  $\Gamma$ . Raising the tem-

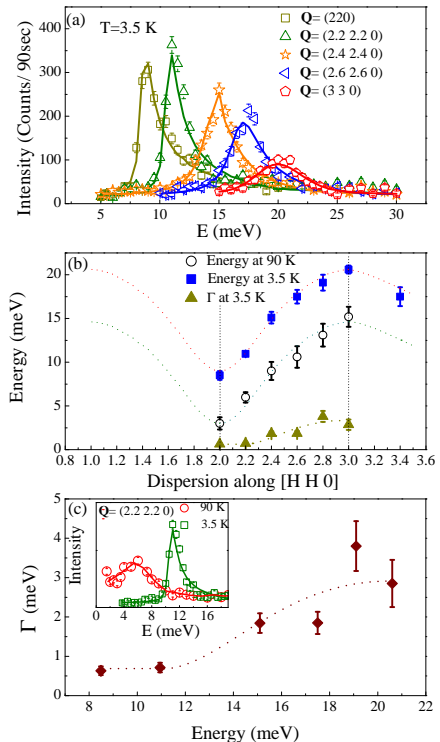


Figure 3: (color online) (a) Constant- $\mathbf{Q}$   $E$  scans at different  $\mathbf{Q}$ 's along  $[H H 0]$  at 3.5 K in  $FeV_2O_4$ . (b) Low-energy Fe spin waves with dispersion along  $[H H 0]$  at 90 and 3.5 K, and the wave-vector dependence of spin wave damping  $\Gamma$  at 3.5 K. (c) Energy dependence of  $\Gamma$  at 3.5 K. The dotted lines are guides to the eye. The inset shows a comparison of the raw data at  $\mathbf{Q}=(2.2 2.2 0)$  at 90 and 3.5 K.

perature usually leads to a gradual spin wave broadening but the clear anomaly at  $T_{N2}$  excludes the thermal effect only. We argue that the spin wave broadening in  $T_{N2} < T < T_{N1}$  originates from strong fluctuations of  $V^{3+}$  spins on the B site in the CFI phase prior to their true canting below  $T_{N2}$ . Such spin fluctuations of  $V^{3+}$  provide interactions with the Fe spin waves and therefore lead to the anomalous spin wave broadening in  $T_{N2} < T < T_{N1}$ .

Representative constant- $\mathbf{Q}$   $E$  scans at various  $\mathbf{Q}$ 's along the  $[H H 0]$  in the NCFI/ferroelectric phase are shown in Fig. 3 (a). The solid lines are the best fit using the model described above and the obtained spin waves dispersions at the two different magnetic states are shown in Fig. 3 (b). Similar to the behavior at the (220) zone center,  $\Gamma$  at each fixed  $\mathbf{Q}$  at 90 K is significantly larger than that at 3.5 K, as shown in the inset of Fig. 3 (c). Compared with the spin-wave spectra of  $MnV_2O_4$  [10, 24], the symmetric lowest-energy spin wave should be the acoustic mode due to the oscillations of Fe spins. Further measurements on other spin wave branches, especially four branches of V spin waves [24] at higher en-

ergies are necessary to obtain accurate magnetic interactions such as  $J_{\text{Fe-V}}$ , in-plane  $J_{\text{V-V}}$ , out-of-plane  $J_{\text{V-V}}$ ,  $J_{\text{Fe-Fe}}$  and the single-ion anisotropies. Note that the spin-wave shapes at 90 K and 3.5 K are very similar with only a shift of  $\approx 5\text{meV}$  indicating that  $\text{Fe}^{2+}$  spins are not influenced obviously below  $T_{N2}$ . This suggests that there is no significant spin frustration at the  $\text{Fe}^{2+}$  site in the NCFI/ferroelectric phase, consistent with powder neutron diffraction results that the direction of the  $\text{Fe}^{2+}$  spins remain along the  $c$  axis below/above  $T_{N2}$ . Therefore, the Fe spins without magnetic frustration at the A site are not mainly responsible for the appearance of the ferroelectricity below  $T_{N2}$ . Instead, the competition between the AFM  $J_{\text{V-V}}$  and AFM  $J_{\text{Fe-V}}$  induces strong spin frustration at the V site resulting in the canting of  $\text{V}^{3+}$  spins, which plays a major role in the appearance of the ferroelectricity based on (extended) spin-current models [25, 26].

As shown in Fig. 3 (b), the spin waves in  $\text{FeV}_2\text{O}_4$  exhibit a significant broadening but without softening at the zone boundary.  $\Gamma \approx 0.7\text{ meV}$  when  $H \leq 2.2$ , but shows a significant increase/step to  $\approx 3\text{ meV}$  above  $H \approx 2.4$ . In Fig. 3(c), the average  $\Gamma/E$  ratio  $\approx 0.11$  is much smaller than that of the metallic ferromagnetic  $\text{La}_{2-2x}\text{Sr}_{1+2x}\text{Mn}_2\text{O}_7$  with  $\Gamma/E \approx 0.33 - 0.46$  [27], consistent with the high insulating behavior of  $\text{FeV}_2\text{O}_4$  [2]. Furthermore, the  $\Gamma/E \approx 0.07$  at the zone center and  $\approx 0.14$  at the zone boundary exhibit weak  $q$  sensitivity of  $\Gamma/E$  and  $\Gamma$  is not linear with respect to  $E$ . All these features exclude magnon-electron scattering [27] as the main mechanism for spin wave broadening. Theoretical calculations [28] have shown that magnon-phonon coupling can increase the spin wave damping without softening the dispersion. Dai *et al.* [29] reported a significant spin wave broadening at the zone boundary with a step in  $\Gamma$  in a few manganese perovskites and demonstrated the role of magnon-phonon coupling as a mechanism of such anomalous broadening. The existence of a strong coupling between spin, orbital, and lattice degrees of freedom [2] and the step in  $\Gamma$  in  $\text{FeV}_2\text{O}_4$  imply that magnon-phonon coupling plays the main role in the spin wave broadening without softening at the zone boundary.

In summary, neutron scattering studies on  $\text{FeV}_2\text{O}_4$  crystal reveal the different roles of two orbital-active  $\text{Fe}^{2+}$  at the A site and  $\text{V}^{3+}$  at the B site in the magnetic excitations. The strong spin-orbit coupling at  $\text{Fe}^{2+}$  A site induces a significant energy gap below  $T_{N1}$  with little contribution from the  $\text{V}^{3+}$ . The absence of a change in energy gap below  $T_{N2}$  is evidence for a very weak SO coupling or significantly quenched orbital moment of the  $\text{V}^{3+}$ . Comparing the Fe spin waves below and above  $T_{N2}$  precludes significant spin frustration at the  $\text{Fe}^{2+}$  site, indicating  $\text{Fe}^{2+}$  may not play an important role in inducing ferroelectricity. The important role of orbital-active  $\text{Fe}^{2+}$  at the A site on the magnetic excitations is expected to be applicable to other spinels with orbital-

active ions at that site, such as  $\text{ACr}_2\text{O}_4$  ( $A = \text{Fe}^{2+}$  or  $\text{Cu}^{2+}$ ). The anomalous spin wave broadening is observed in the collinear ferrimagnetic phase indicative of a possible  $\text{V}^{3+}$  spin fluctuations prior to their true canting in the noncollinear ferrimagnetic phase. The spin wave broadening also exists at the zone boundary without obvious spin wave softening due to magnon-phonon coupling.

## ACKNOWLEDGMENTS

Research at Ames Laboratory is supported by the US Department of Energy, Office of Basic Energy Sciences, Division of Materials Sciences and Engineering under Contract No. DE-AC02-07CH11358. Use of the high flux isotope reactor at the Oak Ridge National Laboratory, was supported by the US Department of Energy, Office of Science, Office of Basic Energy Sciences, under Contract No. DE-AC02-06CH11357.

- 
- [1] Y. Tokura and N. Nagaosa, *science*, **288**, 462 (2000).
  - [2] S. Nizioł, *Phys. Status. Solidi A* **18** K11 (1973)
  - [3] T. Katsufuji, *et al.*, *J. Phys. Soc. Jpn.* **77**, 053708 (2008).
  - [4] S. Sarkar and T. Saha-Dasgupta, *Phys. Rev. B* **84**, 235112 (2011).
  - [5] Q. Zhang, *et al.*, *Phys. Rev. B* **85**, 054405 (2012).
  - [6] G. J. MacDougall, *et al.*, *Phys. Rev. B* **86**, 060414(R) (2012).
  - [7] N. B. Perkins and O. Sikora, *Phys. Rev. B* **76**, 214434 (2007) and references therein.
  - [8] S. Di Matteo, G. Jackeli, and N. B. Perkins, *Phys. Rev. B* **72**, 020408R (2005).
  - [9] H. Tsunetsugu and Y. Motome, *Phys. Rev. B* **68**, 060405R (2003).
  - [10] V. O. Garlea, *et al.*, *Phys. Rev. Lett.* **100**, 066404 (2008).
  - [11] R. Nangneri and S. Y. Savrasov, *Phys. Rev. B* **86**, 085138 (2012).
  - [12] N. Liu, K. H. Zhao, X. L. Shi and L. W. Zhang, *J. Appl. Phys.*, **111**, 124112 (2012).
  - [13] J. W. Lynn, *J Supercond Nov. Magn.*, **13**, 263 (2000).
  - [14] Taka-hisa Arima, *J. Phys. Soc. Jpn.* **80**, 052001 (2011).
  - [15] J.-H. Kim, *et al.*, *Phys. Rev. Lett.*, **107**, 097401 (2011).
  - [16] Y. Nii, *et al.*, *Phys. Rev. B* **86**, 125142 (2012).
  - [17] S. Bordács, *et al.*, *Phys. Rev. Lett.* **103**, 077205 (2009).
  - [18] G. Subías, *et al.*, *Phys. Rev. B* **70**, 155105 (2004).
  - [19] M. Ramazanoglu, *et al.*, *Phys. Rev. B* **87**, 140509 (2013).
  - [20] D. K. Pratt, *et al.*, *Phys. Rev. B* **81**, 140510 (2010).
  - [21] F. Ye, *et al.*, *Phys. Rev. B* **75**, 14408 (2007).
  - [22] A. Zheludev, [www.neutron.ethz.ch/research/resources/reslib](http://www.neutron.ethz.ch/research/resources/reslib).
  - [23] J.-S. Kang, *et al.*, *Phys. Rev. B* **85**, 165136 (2012).
  - [24] J.-H. Chung, *et al.*, *Phys. Rev. B* **77**, 054412 (2012).
  - [25] H. Katsura, N. Nagaosa, and A. V. Balatsky, *Phys. Rev. Lett.* **95**, 057205 (2005).
  - [26] T. A. Kaplan and S. D. Mahanti, *Phys. Rev. B* **83**, 174432 (2011).
  - [27] T. G. Perring, *et al.*, *Phys. Rev. Lett.* **87**, 217201 (2001).
  - [28] N. Furukawa, *J. Phys. Soc. Jpn.* **68**, 2522 (1999).
  - [29] H.Y. Hwang, *et al.*, *Phys. Rev. B* **61**, 9553 (2000).

## SUPPLEMENTAL MATERIAL

### Experimental details

The  $\text{FeV}_2\text{O}_4$  crystal was grown using the floating zone method. The DC susceptibility measurements were carried out on a Magnetic Property Measurement System (Quantum Design, SQUID). A big piece of crystal with the mass  $\approx 1$  g was cut for the elastic and inelastic neutron-scattering measurements that were conducted on the HB3 spectrometer (located at the High Flux Isotope Reactor, HFIR, at Oak Ridge National Laboratory, USA) with a fixed-final-energy ( $E = 14.7$  meV).

### Structural transitions in $\text{FeV}_2\text{O}_4$

Figure 4 (a) shows the splitting of the  $q$  scans of (400) structural Bragg peak in the cubic setting at several representative temperatures. The schematic pictures of distortion of the crystals and the definition of directions of crystalline axes using different settings in different structures are summarized in Fig. 4 (b). At 120 K, one (400) peak splits to  $(220)_T$  and  $(400)_T$  in the tetragonal notation, suggesting the  $c$  axis of the cubic unit cell is compressed due to Jahn-Teller distortion of  $\text{FeO}_4[1-3]$  driven by a ferroic  $\text{Fe}^{2+} 3z^2-r^2$  OO[4] and the cubic structure transforms into high-temperature (HT) tetragonal structure with  $c_c < a_c$  ( $a_c$  is the lattice constant in the cubic phase). As temperature further decreases to 92 K, one of the  $a$  axis in the HT tetragonal phase is compressed[1], resulting in a structural transition to orthorhombic phase, which can be seen from the splitting of two peaks to three peaks  $(400)_O$ ,  $(040)_O$  and  $(004)_O$ . At 50 K, these three peaks evolve back to two peaks, indicating another structural transition to low-temperature (LT) tetragonal phase. As opposed to the HT tetragonal phase, the peak position  $q$  of  $(004)_T$  is smaller than that of  $(220)_T$  peak in the LT tetragonal phase. Moreover, the peak intensity of low- $q$  peak is weaker than that of the high- $q$  peak in the LT tetragonal phase. Thus, the LT tetragonal phase with  $c > a$  is different from the HT tetragonal phase with  $c < a$  and the tetragonal  $c$  axes in these two tetragonal phases are perpendicular to each other in one unit cell. This indicates that the compressed axis ( $b_O$  or  $a_O$ ) in the orthorhombic phase, becomes equal to the  $c_O$ , and therefore, the orthorhombic phase evolves to LT tetragonal phase and the remained axis becomes new  $c$  axis in the tetragonal setting. Based on the above discussion, we notice that during the structural transformation from HT tetragonal phase to LT tetragonal phase in  $\text{FeV}_2\text{O}_4$ , the orthorhombic phase cannot be avoided. It should be noted that as shown in Fig. 1 (a), no change is observed in the  $q$  scans of (400) structural Bragg peak

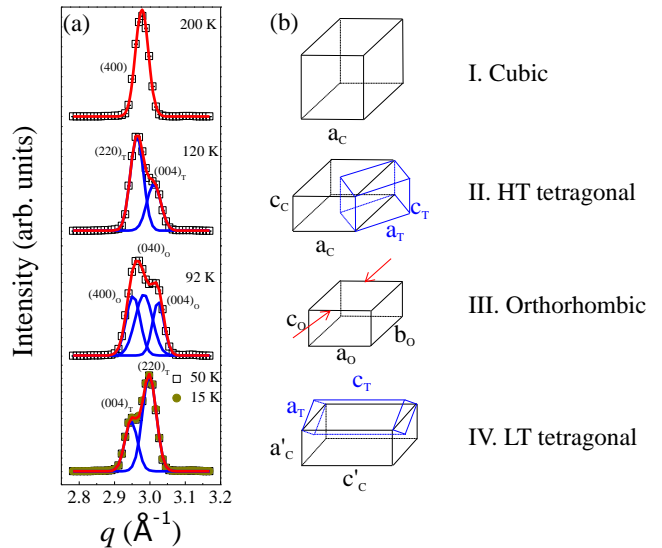


Figure 4: (color online) (a). Splitting of the (400) peak in the cubic setting of  $\text{FeV}_2\text{O}_4$  at representative temperatures. Symbols are experimental data; red lines are the sum of two/three Gaussian fits; blue lines are the single Gaussian fit. (b) Schematic pictures of distortion of the crystals and the definition of directions of crystalline axes in different phases. Note that in both HT and LT tetragonal phases, the unit cell in the tetragonal setting is one half of that distorted from the cubic unit cell above  $T_S$ .

between 50 K and 15 K, excluding any structural transition at around 35 K as reported by Katsufuji *et al.*[1].

It is worthwhile noting that the HT tetragonal-orthorhombic structural transition, accompanied by the paramagnetic-collinear ferrimagnetic transition [3] occurs at 70 K here, consistent with the value in *Ref.* [1], is a little higher than the value of 56 K in the polycrystalline sample [2, 3] and also the value of 60 K [3] or 65 K [4] in the single crystal form, reflecting strong suppression of the nonstoichiometry, i.e.,  $x \approx 0$  in the formulation  $(\text{Fe}^{2+})(\text{Fe}_x^3+\text{V}_{2-x}^{3+})\text{O}_4$  in our crystal since a lower value of  $x$  causes an increase of  $T_{N2}$  [5]. Thus, the investigation on the stoichiometric  $\text{FeV}_2\text{O}_4$  crystal can minimize the effect of nonstoichiometry and reveal intrinsic magnetic excitations.

- 
- [1] T. Katsufuji, T. Suzuki, H. Takei, M. Shingu, K. Kato, K. Osaka, M. Takata, H. Sagayama, and T. Arima, *J. Phys. Soc. Jpn.* **77**, 053708 (2008).
  - [2] Q. Zhang, K. Singh, F. guillou, C. Simon, Y. Breard, V. Caignaert, and V. Hardy, *Phys. Rev. B* **85**, 054405(2012).
  - [3] G. J. MacDougall, V. O. Garlea, A. A. Aczel, H. D. Zhou, S. E. Nagler, *Phys. Rev. B* **86**, 060414(R) (2012).
  - [4] Y. Nii, H. Sagayama, T. Arima, S. Aoyagi, R. Sakai, S. Maki, E. Nishibori, H. Sawa, K. Sugimoto, H. Ohsumi, and M. Takata, *Phys. Rev. B* **86**, 125142 (2012).

- [5] N. Liu, K. H. Zhao, X. L. Shi and L. W. Zhang, *J. Appl. Phys.*, **111**, 124112 (2012).